Physica Medica 57 (2019) 47–57

Contents lists available at ScienceDirect

Physica Medica

journal homepage: www.elsevier.com/locate/ejmp

Original paper

Development of a 3D printed anthropomorphic lung phantom for image quality assessment in CT

Irene Hernandez-Giron[a,*], Johan Michiel den Harder[b], Geert J. Streekstra[b], Jacob Geleijns[a], Wouter J.H. Veldkamp[a]

[a] Radiology Department at the Leiden University Medical Center (LUMC), Leiden, The Netherlands
[b] Academic Medical Center (AMC), Amsterdam, The Netherlands

ARTICLE INFO

Keywords:
Computed tomography
3D printed phantom
Image quality
Lung

ABSTRACT

Purpose: To design a 3D printed anthropomorphic lung vessel phantom for CT image quality assessment and to evaluate the phantom image and dose characteristics.

Methods: An in-house algorithm generated a vessel tree model, based on human lungs anatomy, which was 3D printed using a multi jet modeling printer (0.25 mm ≤ vessel diameters ≤ 8.25 mm) and inserted in an elliptical holder (thorax surrogate).

The phantom was scanned (Toshiba Aquilion Genesis CT) and compared in terms of attenuation (Hounsfield units, HU) and dose characteristics with studies of five patients (normal BMI) and a commercial torso phantom, performed with the same thorax protocol. The pixel value distribution in the lung area was assessed with histograms. To investigate the adjustment of tube current modulation, tube load and CTDI were compared.

Results: The histogram peaks for respectively vessels and surrounding tissue were at 105 HU and −985 HU (3D printed phantom), at −25 HU and −1000 HU (torso phantom) and at 25 HU and −875 HU (average patient). The contrast between vessels and surrounding was −1090 HU (3D printed), −975 HU (torso phantom), and −900 HU (average patient). The measured HU values (soft tissue and vertebra) were (32 ± 15) HU and (210 ± 71) HU (average patient); (4 ± 4) HU, (390 ± 39) HU (torso phantom) and (119 ± 5) HU, (951 ± 31) HU (3D printed phantom and holder). CTDIvol was (1.9 ± 4.7 mGy) for patients, 1.9 mGy for the torso phantom and 2.1 mGy for the 3D printed lung phantom.

Conclusions: An anthropomorphic 3D printed lung phantom was developed and its CT image and dose characteristics evaluated. The phantom has the potential to provide clinically relevant and reproducible measures of CT image quality.

1. Introduction

Computed tomography (CT) is a versatile medical imaging modality, with applications spanning over a wide range of fields [1]. The ample availability of CT scanners together with the continuous growth of the amount of CT scans performed per year worldwide has turned CT into the biggest contributor to the collective radiation dose, representing roughly half of the contribution of medical imaging both in Europe and the USA [2,3]. One of the advances in CT in the past decade, was the introduction of iterative reconstruction (IR) algorithms in the clinical practice. These algorithms have the potential of providing improved image quality compared to traditional filtered back projection (FBP) at the same dose level [1,4].

Image quality is frequently assessed in CT using geometric phantoms containing different test objects embedded in a uniform background. Parameters such as noise, contrast, spatial resolution or low contrast detectability can be measured in these phantoms. These methods are useful in terms of measuring a system's stability or testing whether basic system requirements are met. However, iterative reconstruction algorithms have non-linear properties: these algorithms have proved to work differently for different patient sizes, dose levels, and anatomical areas [4–6]. Therefore, with iterative reconstruction, traditional metrics measured in geometric uniform phantoms will not be representative of image quality in patients.

As a consequence, there is a need for anthropomorphic phantoms that can be combined with objective methods to assess image quality in CT in conditions similar to clinical practice. These phantoms should incorporate the influence of anatomical texture of tissues and reflect the

* Corresponding author.
E-mail address: I.Hernandez_Giron@lumc.nl (I. Hernandez-Giron).

https://doi.org/10.1016/j.ejmp.2018.11.015
Received 10 July 2018; Received in revised form 31 October 2018; Accepted 21 November 2018
Available online 20 December 2018

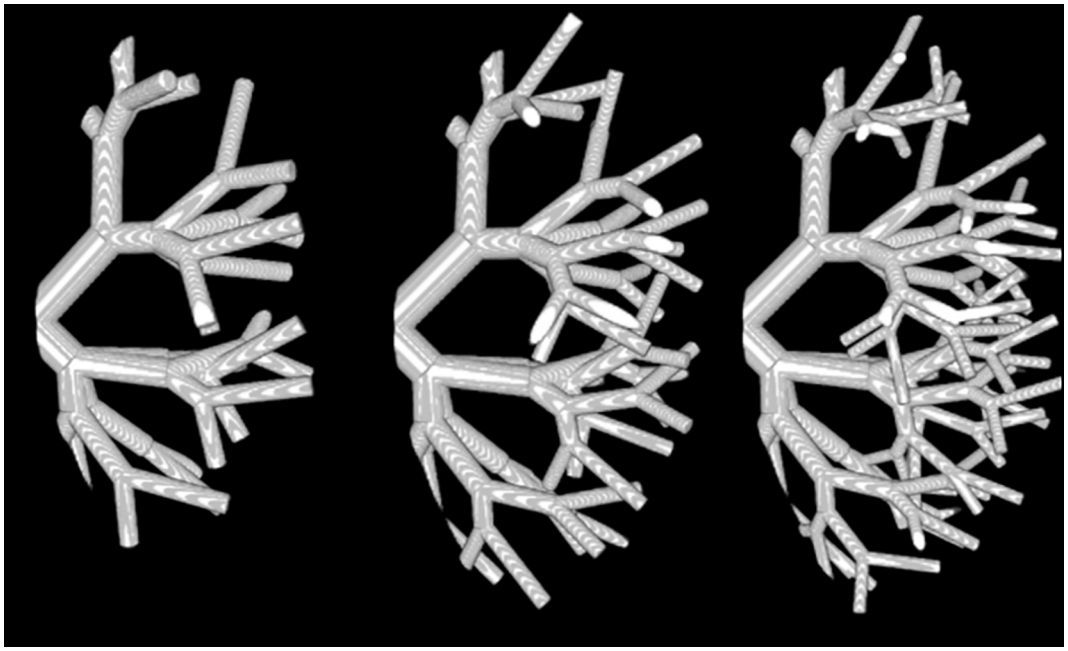

Fig. 1. Depiction of three different generations of the vessel growth algorithm in a rendered 3D view, showing 64 (left), 128 (center) and 256 (right) vessels, respectively.

patient shape and attenuation to some degree.

Anatomically realistic phantoms are commercially available for image quality assessment providing detailed anatomy and attenuation properties comparable to human tissue. A disadvantage of these phantoms is their high cost [7]. An increasingly popular alternative to develop affordable phantoms for image quality assessment in medical imaging is 3D printing [8–11]. This approach enables flexibility of design, reduced costs and the knowledge based on the design files that provides a reference standard for the objects [12]. Besides, very finely detailed structures can be created with certain 3D printing techniques which are not feasible with the traditional commercial anthropomorphic phantoms. Due to these advantages, 3D printing has applications in patient specific prosthesis manufacturing, custom bolus in radiotherapy, surgery planification and phantom development for image quality assessment.

We used 3D printing to generate a CT phantom for measuring the quality of CT images by modeling the vascular system of the human lung. The resulting phantom was used in recent work for image quality assessment with respect to different reconstruction methods [13]. In the work presented in this paper we describe the design and realization of the phantom in detail and investigate its CT imaging and dose characteristics. For this purpose, the phantom was compared to patients and a commercially available anthropomorphic phantom for CT imaging.

2. Materials and methods

2.1. Phantom design and realization

2.1.1. Vessel tree model

The design of the lung vessel tree topology and vessel diameter values along the different branches was based on the work by Weibel et al, which hinged on a thorough microscopic study of lung specimens [14,15]. In these studies, the architecture of primarily the airways was described quantitatively as structures that bifurcate iteratively in smaller structures or segments. Here it should be noted that the blood vessels of the human lung show strong similarity to the airways structure meaning that the diameter and length of vessel segments in each iteration step i is comparable to the airway diameter and length in the corresponding iteration step (both decreasing iteratively). In this study the vessel segments are modelled as cylinders with diameter $d(i)$ and length $l(i)$. The diameters are determined based on the work by Weibel [14,15] by the equation:

$$d\ (i) = d(i-1)\cdot\alpha_d, \tag{1}$$

where $i = 1, 2, .., N$ and $N = 14$ is the maximum number of iterations considered in the study. The largest vessel segment diameter at the root of the tree $d(0) = 10$ mm. The scaling factor α_d remains constant for the larger vessels ($\alpha_d = 0.79$) and changes to 0.944 for the smaller vessels [14,15].

In a similar way, the length of the segments is modeled according to:

$$l\ (i) = l(i-1)\cdot\alpha_l, \tag{2}$$

where $i = 1, 2, \ldots, N$ and $N = 14$. The largest vessel segment length at the root of the tree $l(0) = 15$ mm and the reduction factor α_l is 0.85 for the larger vessels and 0.944 for the smaller vessels, respectively [14,15].

Software was developed in MATLAB® (MathWorks®, Natick, MA) to generate the lung vessels inside an elliptically shaped frame with a limited height to maintain low production cost and to facilitate transport and handling (frame dimensions were 150 × 103 × 26 mm, i.e. ellipse major axis × ellipse minor axis × frame height). A seed point was placed left at the short axis of the elliptical frame, for a main vessel with 10 mm diameter $d(0)$. At the seed point, the algorithm immediately split it into two massive cylinders representing the next generation vessels of 8.5 mm diameter $d(1)$ and of 12.75 mm in length $l(1)$. The end point of each vessel segment was used either as a bifurcation point to start two new segments or as a starting point for an elongation of the same segment, increasing the chance of bifurcation after each elongation step. After each bifurcation, the direction of the two branches was chosen at random but constrained to be within a 45° angle with respect to the direction of the parent vessel [14,15].

In this way, a 3D distribution of the vessels was created in 14 generations, resulting in segment diameters down to 0.25 mm. The total number of generated vessel segments was in the order of 20,000. Fig. 1 depicts some of the stages of the vessel growth during the simulation.

2.1.2. 3D printing of the vessel tree model

The generated binary lung phantom model, was transformed into a

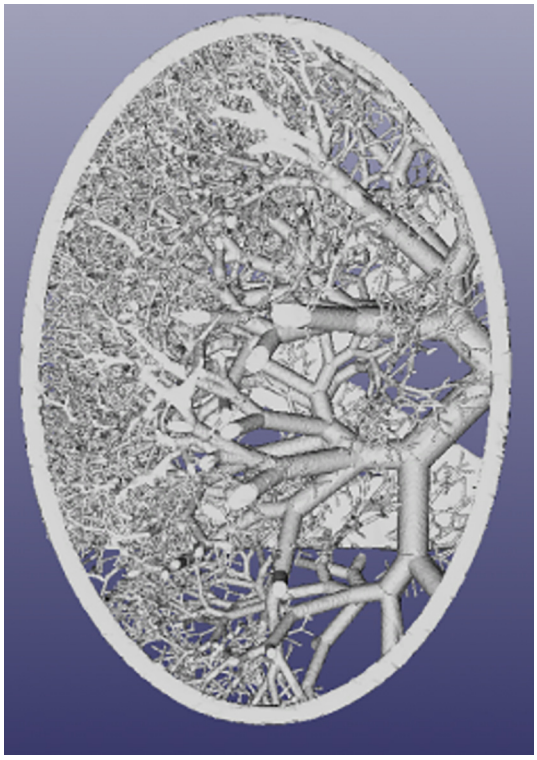

Fig. 2. A rendered 3D view of the STL design file of the lung vessel phantom used as input for the 3D printer.

Standard Tesselation Language (STL) file, which is generally used as input by 3D printers. First, the binary phantom model was uploaded into the software application 3D slicer [16] to generate a mesh model. A volume rendering of the 3D model, as it appears in 3D slicer, can be seen in Fig. 2. Then, the software package Meshlab [17] was used to rescale the model and clean it, removing possible unreferenced vertices, non-manifold edges, and null faces that may in general occur as a result from the conversion process into the STL file format.

Using the STL file as input, the phantom was printed in a ProJet HD 3000 3D printer applying the multi jet modeling (MJM) technique and ultrahigh definition mode (UHD) (32 μm layer thickness, resolution 656 × 656 × 800 DPI (xyz), accuracy 0.025–0.05 mm per inch of part dimension), which was appropriate for the fine details and smooth surfaces that were required for the vessel model. As a design criterion of the phantom, the size of the smallest structures was 0.25 mm, below the resolution of the latest generation of commercial CT systems (~0.5 mm). The material used by this printer and technique was Visijet EX200 (density 1.1 $g{\cdot}cm^{-3}$ in solid state). The 3D printed material was deposited layer by layer and cured using UV light, together with a wax based support material which helped to create scaffolding for the model. The support material was removed afterwards in an oven, which melted it without damaging the model. The final 3D printed lung phantom, of dimensions 150 × 103 × 26 mm, can be seen in Fig. 3. The wall thickness of the oval frame encircling the vessels was 4 mm.

2.1.3. Thorax shaped holder

To mimic the attenuation and shape of the patient's thorax, a polymetyl methacrylate (PMMA) elliptical holder was designed using the design freeware Freecad 0.14 and produced with dimensions 300 × 200 × 29 mm (Fig. 3) [18]. These dimensions are representative for a human thorax. The design included two elliptical holes to fit the lung phantom and a cylindrical gap to insert a polytetrafluoroethylene (PTFE) cylinder with a diameter of 33 mm to mimic the patient's spinal column attenuation. Teflon is used as a surrogate for dense bone in several commercial image quality phantoms.

2.2. Image acquisition

The CT-values and dose characteristics of the 3D printed lung phantom were compared to those of a commercial torso phantom and patients.

The commercial phantom used in the study was the CT Torso phantom (CTU-41, Kyoto Kagaku Co. Ltd, Japan), which mimics the head and torso anatomy of an adult Japanese male, using synthetic bones (cast on different types of epoxy resins) and soft tissue (based on urethane resins), and mimicking the attenuation of organs [19]. It reproduces the lung vessel tree up to the fourth branch generation (made of urethane base resin, density 1.06 $g{\cdot}cm^{-3}$). The height and weight of this phantom is 100 cm and 45 kg, respectively, and the phantom does not have arms or legs [7,19,20].

Five patients, imaged with the same CT protocol, were selected from PACS, using as inclusion criterion that they had normal body mass index ($18.5 \leq BMI \leq 24.9\ kg/m^2$) and as exclusion criterion diagnosed disease in the parenchyma and pulmonary vessels. The five patients (three women, two men) had ages ranging between 19 and 71 years (46.0 years average).

All image acquisitions were performed with a Toshiba Aquilion ONE GENESIS Edition CT scanner with a high resolution thorax protocol. For comparison between the patients and the phantoms, only the patient images resulting from the helical acquisition during inspiration were used. During this phase, the air content in the lungs is maximal, making the comparison with the commercial torso phantom and the 3D printed phantom more consistent, as these do not have a surrogate for parenchyma but only air. The acquisition parameters were 120 kV, 0.275 s rotation time, 80 × 0.5 mm beam collimation, pitch of 0.813, the tube current modulation was activated (Sure Exposure, SD = 10.00) and contrast agent was not administered to the patients. The reconstructed image series consisted of slices of 1 mm thickness and 1 mm image interval, using AIDR 3D enhanced and FC08 (body standard volume) as reconstruction algorithm and filter, respectively.

The set of images for the 3D printed phantom consisted of 23 images after discarding the starting and ending slices, which presented artifacts. Due to the limited length of the 3D printed phantom's image data set in this study (23 mm in the z direction), it was decided to select a range of images from the patients and commercial torso phantom sets of the same length taken around the same anatomical location, specifically starting 2.5 cm below the carina, as advised by a senior radiologist. Thus, subsets of 23 mm length (23 images, 1 mm slice thickness) were available for the five patients, the commercial torso phantom and the 3D printed phantom. Fig. 4 shows the central slice of the selected volumes for one of the patients (A), the anthropomorphic commercial torso phantom (B), and for the 3D printed lung phantom (C).

2.3. Phantom evaluation

CT scan data of the 3D printed lung phantom were compared to a commercial torso phantom and patients with regard to three main aspects: (1) ROI measurements of CT-values to investigate the characteristics of the materials in the phantoms versus corresponding patient anatomy, (2) histogram analysis of HU values to assess the distribution of CT-values in the lung area for vessels and vessel surrounding, and (3) dose characteristics, i.e. tube load (mAs) and CTDI (mGy). Additionally, to estimate the 3D printing process accuracy of one of the biggest vessels (8.5 mm diameter) was measured with a Vernier caliper (± 0.05 mm accuracy) in three different positions along the vessel.

2.3.1. ROI measurements

First, the characterization of the attenuation properties of the materials used in the 3D printed lung phantom and thorax holder (Visijet EX200, PMMA and Teflon) was performed. Regions of interest (ROIs) were drawn using ImageJ at different positions in the patient images

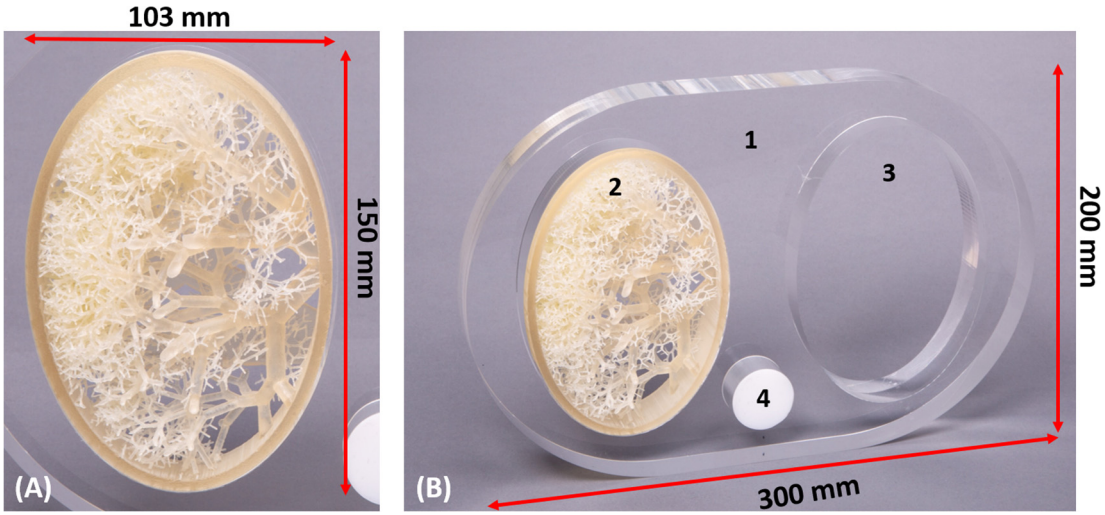

Fig. 3. The 3D printed lung vessel phantom (A) contains vessels with a diameter ranging from 10 to 0.25 mm. In (B), it was placed into a PMMA chest phantom container (1), with two holes (right lung (2), left lung (3)) and a Teflon insert (3) as a surrogate for the spine, to mimic the anatomy of the patient's chest.

(Fig. 5; indexes 1 to 4 express different tissues) [21]. Comparable ROIs were drawn in the commercial torso phantom images and in the images of the 3D printed phantom. ROIs represented vessels (1), vessel surrounding (2), soft tissue (3), and bone/vertebra (4). In the 3D printed phantom with thorax holder, indexes 1–4 relate to: Visijet EX200, air, PMMA, and PTFE, respectively.

For all the ROIs, except the vessels and the vessel surrounding, the 23 available slices were taken into account and the mean Hounsfield Unit (HU) was calculated. For the patients, ROI results were averaged over the 5 patients. Care was taken not to include more than one tissue per ROI in a patient.

For the vessels, five ROIs were taken in the biggest vessels. For each vessel considered, one ROI was drawn in its central slice, to avoid including the parenchyma in the measurement. Fig. 6A, B and C show examples for one vessel in a patient, in the commercial torso phantom and in the 3D printed phantom, respectively. Similar to the vessels, also for the vessel surrounding or parenchyma, five ROIs were taken in patients and in the two phantoms respectively and average HU values calculated.

Additionally, the attenuation properties of the 3D printed material used for the lung vessel phantom and those used for the thorax holder (PMMA, Teflon, air), were measured empirically for the X-ray energy range available in the scanner. Scans were performed with the same high-resolution thorax protocol varying the selected kV (80–100–120–135 kV). The same methodology and regions of interest (as in Section 2.3.1) were selected to calculate the average HU per material for each kV. These acquisitions were performed at a constant dose, for all kVs, varying the selected mAs value.

2.3.2. Histogram analysis

Normalized histograms (number of pixels for each gray level, normalized by the total number of pixels) were calculated over the stacks of 23 image slices (range (−1145 HU, 250 HU); 5 HU bin size) in ImageJ software [21]. For the patients the average histogram was determined over the 5 patients. The histograms were calculated in ROIs matching the entire lung area in each slice. Since for patients and the commercial torso phantom the lung area (of the right lung) was not defined in advance, ROIs were obtained by automatic threshold segmentation [22]. The histograms reflected the number of pixels of specific CT-values in proportion to the total number of pixels in the lung area. In this way, the histograms provided information on the proportion of vessels and vessel surrounding in the lung area.

Finally, the histogram of the 3D printed lung phantom was compared to the histograms of the patients and the commercial torso phantom. For this purpose, the gray level distributions of the histograms were divided in two parts: one in the range (−1145 HU, −500 HU) and the other in the range (−499 HU, 250 HU). The first part contained the maximum peak related to vessel surrounding (air or parenchyma) and the second part contained the peak related to the lung vessels. This separation in two regions helps the visual comparison of histograms.

2.3.3. Power spectrum analysis

Power spectrum analysis was performed to compare the signal patterns related to the vessel distributions. Samples (four volumes of interest in each, at different locations, (64 × 64 pixels, 23 images per volume) were subtracted from the right lung field of one of the patients, the commercial torso phantom, the 3D printed lung phantom and additionally inside the empty insert space of the PMMA thorax shape holder to have air as a reference. These samples were analyzed in ImageJ [21] selecting the Fast Fourier Transform and the Raw power spectrum option to illustrate the signal patterns.

To perform a quantitative power spectrum analysis, the 92 samples available per set (patient, commercial torso phantom, 3D printed lung phantom and air) were combined and analyzed using in-house code developed in Matlab to calculate the radially averaged power spectrum.

2.3.4. Dose assessment

A dosimetric comparison was carried out. The selected high-resolution lung protocol used tube current modulation. The mAs per slice was derived for patients and phantoms from the DICOM meta data and finally averaged over the 23 slices in consideration. The $CTDI_{vol}$ related to the 23 slices was derived from this average mAs based on the linear relation between $CTDI_{vol}$ and mAs.

For further interpretation of the $CTDI_{vol}$, the dimensions of the 3D printed phantom were compared to equivalent values obtained in the commercial torso phantom and patient images, in particular for the right lung and the thorax. For this, the external shape of the right lung section and the patient thorax were segmented in each of the images available using ImageJ as shown by the red inner and outer regions, respectively, in Fig. 4A [21,22]. The obtained regions of interest were fitted to ellipses to estimate the sizes of the lung and the thorax (minor and major axis) and to compare them to the 3D printed phantom and the PMMA holder.

2.3.5. Subjective evaluation of the 3D printed phantom images

A senior radiologist (> 15 years experience in clinical thoracic imaging) evaluated the images used in the present paper for the 3d

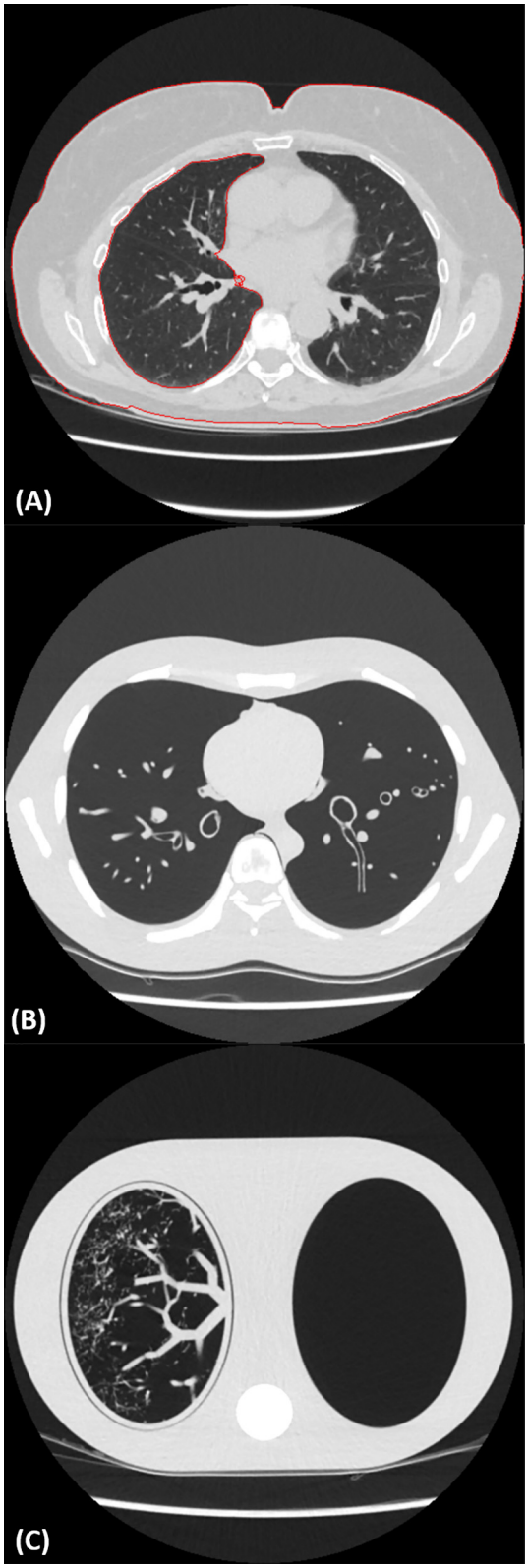

Fig. 4. Image slices shown belonging to a patient (A), the commercial torso phantom (B) and the 3D printed lung phantom (C). Slices for the patient and the torso phantom are selected from the image data set of 23 slices (23 mm) starting 2.5 cm below the carina.

printed lung vessel phantom and the commercial torso phantom compared to patients. Aspects such as the vessel diameters and distribution and contrast were assessed.

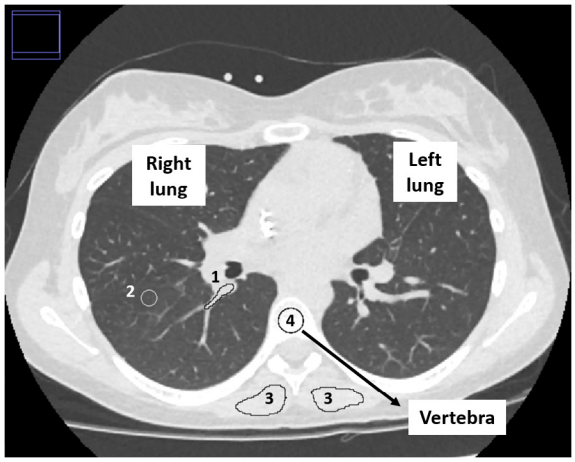

Fig. 5. Regions of interest (ROIs) drawn at different positions/tissues in the central axial slice of the stack of images of a patient. For the commercial torso phantom and the 3D printed thorax phantom ROIs were defined at similar positions. Indexes 1 to 4 express different tissues: vessels (1), vessel surrounding (2), soft tissue (3), and bone/vertebra (4).

3. Results

3.1. ROI measurements

The results of the measurements performed to assess the attenuation (expressed as HU) for the different tissues (vessels and vessel surrounding, vertebra and muscles) and materials used in the phantoms are summarized in Table 1. ROIs were drawn at equivalent anatomical positions in patient images and in images of the two phantoms.

The attenuation properties of the materials used in the 3D printed lung phantom and thorax shaped holder (with the equivalent tissues in patients) were as follows (for each material, the values correspond to 80–100–120–135 kV, respectively): PMMA [soft tissue: (103 ± 4) HU, (118 ± 4) HU, (119 ± 10) HU, (125 ± 8) HU]; Teflon [vertebra: (1100 ± 4) HU, (118 ± 4) HU, (119 ± 8) HU, (125 ± 8) HU]; Air [vessel surrounding, lung parenchyma: (−988 ± 20) HU, (−986 ± 18) HU, (−985 ± 18) HU, (−971 ± 14) HU]; Visijet EX200 [lung vessels: (86 ± 15) HU, (103 ± 18) HU, (104 ± 22) HU, (107 ± 16) HU].

With regard to the materials and tissues considered, the densities for patient tissue and some of the materials used in the phantoms, were retrieved from ICRU-44 and manufacturers documentation [23]. For patients (ICRU-44): vessels (using blood as reference: 1.06 g/cm^3), lung tissue (combination of lung parenchyma and lung vessels: 1.05 g/cm^3), soft tissue (1.06 g/cm^3), cortical bone (1.92 g/cm^3). For the 3D printed lung phantom and thorax shaped holder: vessels (Visijet EX200: 1.10 g/cm^3, solid state), soft tissue (PMMA: 1.19 g/cm^3), bone (Teflon: 2.25 g/cm^3), vessel surrounding tissue (dry air, sea level: 1.205 g/cm^3). For the commercial torso phantom: vessels (urethane base resin EZ50: 1.06 g/cm^3), soft tissue (urethane base resin EZ50: 1.06 g/cm^3), vessel surrounding tissue (dry air, sea level: 1.205 g/cm^3), bones (epoxy base resin, density not available).

3.2. Histogram analysis

The normalized histograms of the pixel value distributions inside the lung section are depicted in Fig. 7A for the 3D printed, commercial phantom and the patients. For the patients, the average patient histogram is shown. Fig. 7B and 7C show zoomed in sections of Fig. 7A, in the range (−1145 HU, −500 HU), which corresponds to the vessel surrounding (7B) and in the range (−500 HU, 250 HU) which corresponds to larger vessels, (Fig. 7C). In the histograms, the peak for the percentage of pixel values related to the surrounding tissue or

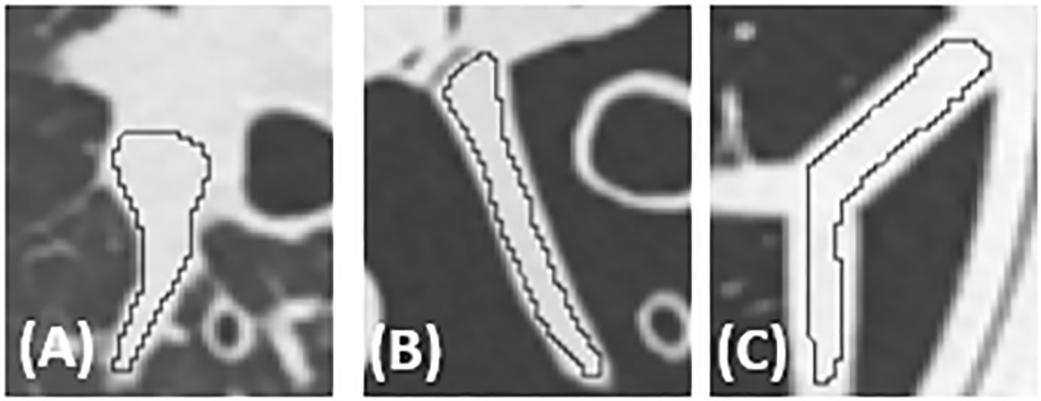

Fig. 6. Examples of vessels and the ROIs (black line) used to measure their attenuation in a patient, the commercial torso phantom (B) and the 3D printed lung vessel phantom (C). Images are displayed with (WL/WW = −600/1600 HU) and equal zoom settings.

parenchyma is roughly one order of magnitude higher than the peak related to the vessels.

Fig. 8 shows the central slice of the image stack for one of the patients (A), the commercial torso phantom (B) and the 3D printed phantom (C) for different window settings. The window settings correspond to the whole range of HUs in the lung parenchyma (−1050 HU, −500 HU) (Fig. 8A-C), and a HU range containing mainly the larger vessels (−500, 250 HU) (Fig. 8D-E). All the images were reconstructed with the same FOV (312.3 mm). The selected ranges correspond to the histograms shown in Fig. 7B-C.

3.3. Power spectrum analysis

Selected examples of the signal patterns related to the vessels obtained in ImageJ are shown in Fig. 9 for the 3D printed phantom, commercial torso phantom, one patient and air, respectively.

Fig. 10 shows the power spectrum results based on the analysis of the samples (92 per condition) subtracted at different locations in the lung tree.

The power spectrum analysis (Fig. 10), showed a variation of the signal patterns depending on the vessel distribution (number of vessels, size and orientation) included in the studied region. When bigger vessels were included, they appeared as high signals in the power spectrum distribution. Compared to the air samples, in both phantoms (3D printed and commercial torso phantom), the power analysis shows higher values, as it is observed in patients. The commercial torso phantom, had whole regions in the lung field totally void of vessels (Fig. 9, top row, fourth column), which made that the power spectrum analysis in those areas was very similar to the one obtained in air, with lower values.

With regard to the radially averaged power spectrum (Fig. 10), it can be seen that the 3D printed lung vessel phantom follows a similar power distribution as in patients and the commercial torso phantom, with power spectrum values in the same order of magnitude. Overall, the 3D printed phantom showed slightly higher values than the patient and the commercial torso phantom. The samples taken in air, used as a reference, showed power values several orders of magnitude below the patient and both phantoms, as expected.

3.4. Dose assessment

Regarding the dose comparison between the 3D printed lung phantom, patients and commercial phantom, the results are summarized in Table 2. Values given for mAs and $CTDI_{vol}$ refer to the 23 slices in consideration for patients and phantoms.

3.5. Subjective evaluation of the 3D printed phantom images

The evaluation of the senior radiologist that analyzed the 3d printed lung vessel phantom CT images, compared to the commercial torso phantom and patients, can be summarized as follows: the 3D printed lung phantom only represents the arterial tree, not veins or bronchial tree. The main artery, lower lobe artery and segmental arteries are a good representation of patients' anatomy, in terms of diameters and distribution, especially in the z-direction. The proximal vessels, closer to the heart, are bigger in patients, but this was not considered a relevant limitation. As a branching model of the arteries, it was estimated as realistic. As a remark, in patients, the subpleural area is empty of vessels in the last centimeter, whereas in the phantom, this area is rather populated with small vessels. The absence of lung parenchyma makes the contrast of the vessels higher than in patients (in scans without contrast injection). With regard to the commercial torso phantom, the evaluation was as follows: It represents vessels and also airways to certain extent, though the airways walls were considered too

Table 1
Measured mean pixel value (MPV, expressed in HU), standard deviation (σ) for the different samples (average area (min–max)) of tissues or materials for the patients, the commercial torso phantom and the 3D printed lung phantom (with the PMMA thorax holder). In the 3D printed phantom with thorax holder, index 1–4 relate to: Visijet EX200, air, PMMA, and PTFE, respectively.

		Average patient			Torso phantom			3D printed lung phantom		
	ROI	Area (mm^2)	MPV (HU)	σ (HU)	Area (mm^2)	MPV (HU)	σ (HU)	Area (mm^2)	MPV (HU)	σ (HU)
Vessels	1	77.1 (55.2–170.5)	5	12	67.9 (45.2–96.3)	−26	6	111.2 (72.5–144.0)	104	11
Vessel surrounding	2	82.6 (46.5–157.7)	−884	17	125.2 (80.1–165.1)	−998	3	116.5 (77.4–160.4)	−985	9
Soft tissue	3	312.0 (213.5–415.2)	32	15	305.7	4	4	320.5	119	5
Vertebra	4	301.4 (241.0–325.8)	210	71	190.8	390	39	289.9	950	31

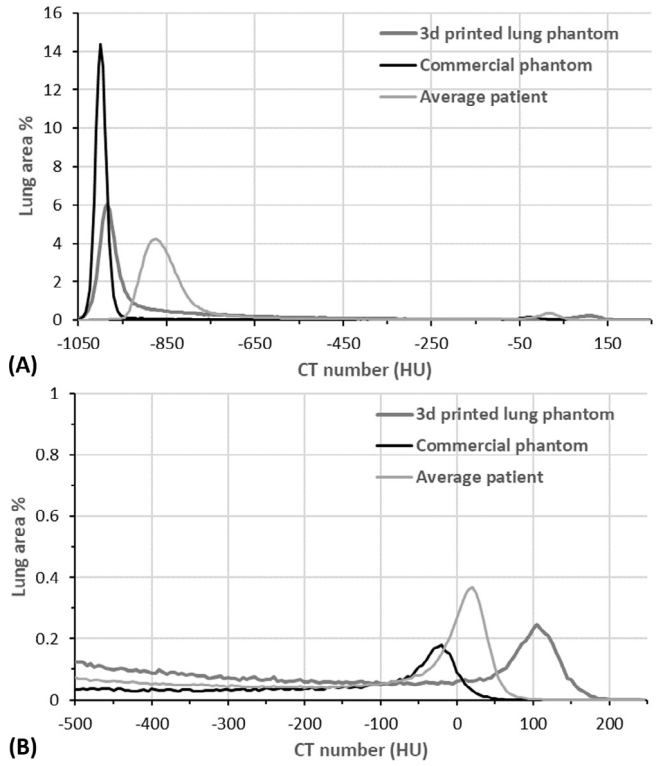

Fig. 7. Normalized histograms (percentage of cumulative total lung area over the image stack) from the gray level distributions inside the lung section for the average patient (median lung area over patients), 3D printed lung phantom and commercial torso phantom. (A) Shows the global histogram inside the lung section and (B) zooms-in the part corresponding to the vessels, between (−500 HU, 250 HU), the histograms peaks correspond to the distribution of pixel values for the vessels ~(−50 HU, 150 HU range) and the surrounding tissue ~(−1000 HU, −700 HU range), respectively.

thick compared to patients. For the vessel distribution, it presents less complexity than in patients and the 3D printed phantom and is limited to the fourth bifurcation. This phantom has relatively few peripheral vessels, which is apparent, especially when scrolling in the z-direction. The branching was considered slightly smoother (and thus more similar to patients) than in the 3D printed vessel phantom. The absence of parenchyma also makes the vessels contrast higher than in patients.

4. Discussion

This work showed that a phantom mimicking complex anatomical structures, using information from published anatomy data, can be designed and manufactured using 3D printing for the purpose of image quality assessment in CT. Software was developed in house to generate a vessel tree model based on the work by Weibel et al, assuming a fractal behavior. The diameters of the vessels in the printed phantom ranged between 8.5 mm and 0.25 mm, the smallest being below the resolution of typical modern state of the art CT systems [1]. Published data by Huang et al, based on human post-mortem lungs, showed up to 15 vessel generations between the main arteries and capillaries, with diameters down to 0.02 mm [24]. The smallest 3D printed vessels in the phantom, which corresponded to the highest resolution in the selected 3D printed, fall in the range of diameters of order 6 vessels (0.22 mm diameter), as described in Huang et al. [24].

The lung phantom was compared to patient data and a commercial torso phantom. The visual comparison of the obtained images with the HRCT thorax protocol (Fig. 7) depicts that the fine vessels and structures of the 3D printed lung phantom are more similar to patient images than the commercial torso phantom, which only contained vessels until the fourth bifurcation. There is no additional published data about the model used to create the vessel vascular tree in the commercial torso phantom, in terms of lengths, diameters or branching, which hinders further comparison with the 3D printed lung phantom.

The images of the phantoms and patients were compared in terms of size, using segmentation software to obtain the external and internal dimensions of the thorax and the lung sections. As shown in Table 2, the horizontal and vertical dimensions of the 3D printed phantom are of the same order as the lung in patients and in the torso phantom in the reference anatomical location below the carina. The right lung section area in the average patient and in the commercial torso phantom was, within the confidence interval, comparable to the 3D printed lung phantom. In terms of dose, for both the commercial torso phantom and the 3D printed phantom, the CT system selected a similar tube current per rotation as for the smallest patients in this study. It has to be noted that in this study, only one 3D printed insert for the lung was included, while the other hole in the thorax holder remained empty. It is to be expected that when two inserts are included as surrogates of the lung, the total attenuation and thus the dose will be closer to the settings for patients. The phantom and the PMMA holder currently represent a small patient within the range of normal BMI (BMI ≈ 19 $kg \cdot m^{-2}$), as well as the commercial torso phantom. This can be modified by changing the dimensions used for the external PMMA holder mimicking the thorax or selecting a different material as surrogate of the soft tissue in the patient.

The attenuation of the material used to print the vessel phantom (Visijet EX200) was higher than the attenuation observed in patients, whereas in the commercial torso phantom it was lower (Table 1). Finding 3D printing materials that show attenuation properties similar to human tissue is currently being investigated by several groups [10,25–28]. New materials are constantly being developed by 3D printing companies. An interesting feature present in most 3D printers is the so called infill density. This parameter is usually modified to save printing material and thus reduce costs. For a model, the outer shape can be printed solid, whereas the inside can be printed as a grid with different ratios between material and air (infill density). Kairn et al modified the infill factor to create surrogates for different tissues based on the same 3D printed material (ABS), including lung tissue in a particular printer, but the resolution was limited to the minimum wall thickness allowed by the printer to make the model robust (1 mm) [27]. Accurately controlling this factor or changing it on the fly during the printing process might allow to obtain custom attenuation values for different parts of the phantom, provided that the grid structures are smaller than the resolution of the CT detector, but this function is not available in the current 3D printers on the market [10].

Kapetanakis et al, addressed that printed patterns might be induced in the printed objects (which will depend on the printing technique and material of choice) which can be an issue for applications for phantoms [29]. In their paper, a phantom for image quality in mammography was printed using polylactic acid (PLA) and Fused Filament Deposition Modelling (FDM) as printing technique, in which the plastic filament, is melted and deposited in a predefined path layer by layer. For the lung vessel phantom, multijet modelling was selected, which can be seen as similar to a 2D desktop printer with multiple printheads: droplets of photosensitive material (in this case in liquid form) are deposited and solidified with UV light layer by layer. This technique enables to create objects with high level of detail and smooth surfaces, minimizing possible pattern issues as those addressed in Kapetanakis et al. [29].

The histogram analysis showed differences between the 3D printed phantom and patients. The most noticeable one is that the first peak in the histogram is shifted to lower attenuations, due to the lack of a surrogate for parenchyma. This shortcoming is also shared by commercial phantoms, such as the commercial torso phantom used in this study and the Multipurpose Chest Phantom N1 (“Lungman”, also manufactured by Kyoto Kagaku), which to our knowledge is the most detailed phantom with regard to the lung vessel tree commercially

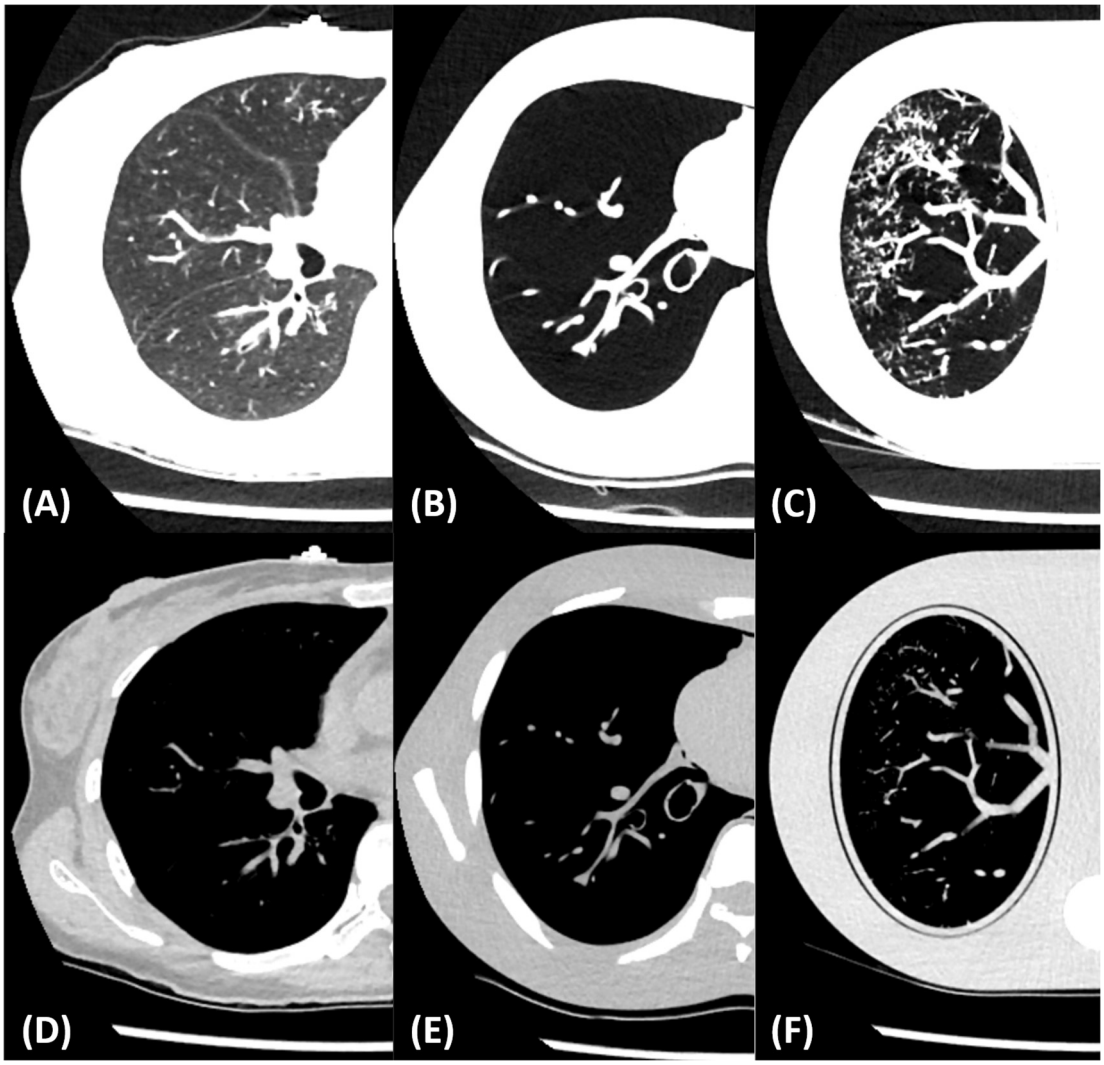

Fig. 8. Selection of images for one of the patients (A, D), commercial torso phantom (B, E) and 3D printed phantom (D, F), reconstructed with a FOV = 312.3 mm, after applying different window settings. Top row emphasizes the parenchyma and small vessels (WL/WW = −800 HU/500 HU), bottom row depicts major vessels and soft tissue (WL/WW = −175 HU/750 HU).

available on the market [28]. This limitation makes the visibility of the nodules more conspicuous than in patient images. Some research groups and a few commercial thorax phantoms (without vessels) have used foam, sponge and low attenuation materials to overcome this, but not in combination with detailed structures like those used in the 3D printed lung phantom [30–33].

There exist other published branching models for the lung strutures. Kitaoka et al published a branching model for the lung airways based on two major principles: the fluid amount delivered through a branch and the volume of the supplied region are proportional and the terminal branches in the organ are homogeneously arranged [34]. The model, aimed at studying structure-function in the lung, included nine basic rules and four additional complementary rules, which makes it more complex than the branching model proposed by Weibel. Burrowes et al proposed geometric models of the arterial and venous trees, based on skeletonization of patient CT images combined with a volume-filling braching algorithm and an empirically based model for the supernumerary vessels [35]. Abadi et al, developed a branching algorithm to generate vessel and bronchial trees to be combined with existing virtual phantoms, the XCAT family, simulating patients of both sexes and an age range [36]. Further developments in lung vasculature models as these, could be implemented in the framework proposed in this paper, to develop other anatomically accurate 3D printed phantoms as surrogates for the vascular trees of the lung or other organs.

A 3D printed lung phantom was developed by Solomon et al also for CT image quality assessment. Their phantom was shaped as a disk of 16.5 cm diameter and 3 cm height, with a 3 cm diameter hole in its center, to be used as an insert in a commercial phantom [11,13]. Their vessel model placed seeds around the central disk which developed into segments of vessels with a limited range of diameters (between 2 and 2.5 mm) and lengths (between 13 and 18 mm), chosen at random. Our approach in the phantom design simulated a section of the vascular tree of the lung, with a geometrical distribution of the vessels, starting at one side instead of the center, which is more realistic compared to human lungs. The in-house lung model in our study was designed to generate a much wider range of vessel sizes (diameters between 8.5 mm and 0.25 mm). Very small details can be achieved with certain 3D printing techniques (like multijet modelling), which has the advantage of being able to create test objects containing structures below or close to the resolution and performance capabilities of the state of the art CT systems.

With regard to the materials used for the phantom, the lung model by Solomon et al was printed in an Object Connex printer (Stratasys Ltd), with the Polyjet technique, which enables to print several materials simultaneously. The vessels, the external disk to support them and objects of different shapes as surrogates for lung nodules were printed

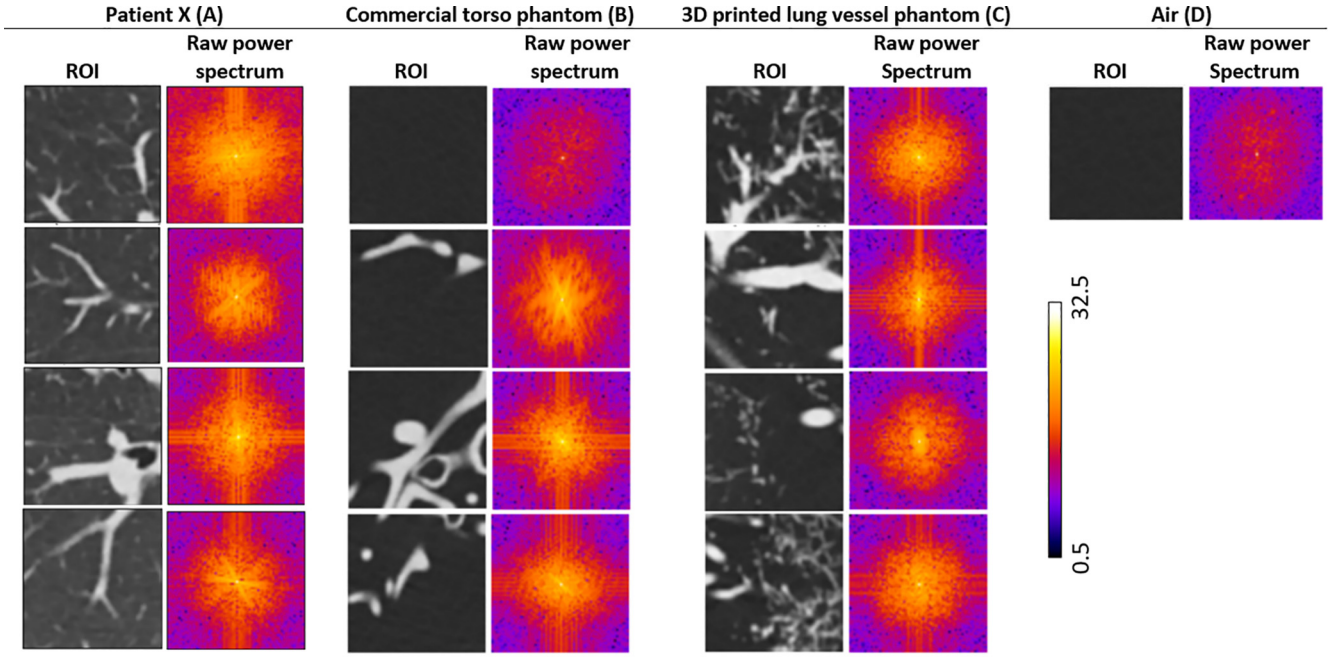

Fig. 9. Visual examples of the raw Power Spectrum (logarithmic scale) measured over samples (64x64 pixels) containing lung vessels from a patient (9A), commercial torso phantom (9B), 3D printed lung vessel phantom (9C) and air (9D).

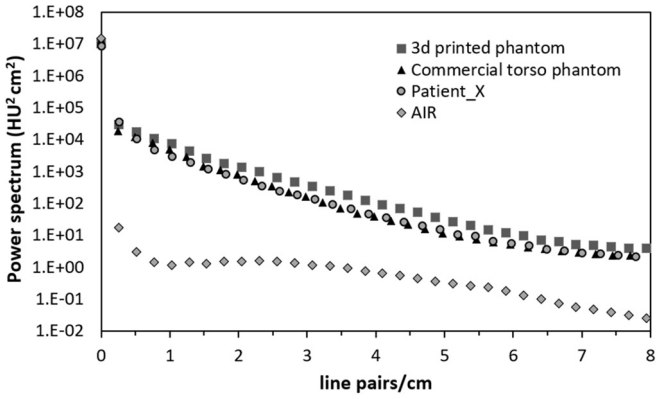

Fig. 10. Power spectrum (log scale) for one of the patients, the 3d printed lung phantom, the commercial torso phantom and air, based on the analysis of 92 samples (64 × 64 pixels) subtracted from the respective image sets, in the lung field region.

simultaneously using the materials Durus White (vessels) and Vero White (outer holder and nodules), with attenuations of 70 HU and 88 HU, respectively at 120 kV. The lung phantom presented in this work was printed with VisijetEX200 with an attenuation of ~105 HU. These values are higher than those measured in patients for the vessels (~15–25 HU) as found in the histogram analysis performed in our study (Fig. 7).

The attenuation of the 3D printed material selected for the lung vessel phantom (Visijet EX200) increased with increasing kV (~21 HU between 80 and 135 kV), based on measurements taken on the bigger vessels. This increase with kV is consistent with the findings of Solomon et al, with an increase in the HU number of ~30 HU in the range 80–140 kV for the material (Durus White) used in their lung vessel phantom [9].

The development of new 3D printed materials and the study of their properties to achieve the desired attenuation matching patient tissues (at the energies used during image acquisition for different modalities) is an active path of research [37,38]. Some low density materials (in the range of water) could be good candidates for the lung vessels in the phantom. For instance, in Ivanov et al, a wide variety of 3D printed materials of different types (resins, PLA, ABS and nylon, among others, were studied as possible surrogates for breast tissues (adipose, glandular and skin) for typical effective energies used in mammography [37]. For instance, according to the values shown in that study, the attenuation coefficients of ABS, ABS_LAB and Nylon_LAB (μ values of 0.204, 0.191, 0.214 g/cm^2 at 60 keV effective energy) have attenuation coefficients close to water (μ = 0.206 g/cm^2), which is similar in

Table 2
Measured sizes of the right lung field and the thorax (averaged over the region selected referenced to the carina) for the commercial phantom and the five patients in the study, in comparison to the defined dimensions with regard to the 3D printed phantom. The $CTDI_{vol}$ and the average automatically selected mAs are also shown together with the body mass index (BMI), sex and age of the patients. The errors are given as one standard deviation (when its error = 0, it is because in this section, mAs did not change during the acquisition in range taken with the carina as a reference).

	Patient 1	Patient 2	Patient 3	Patient 4	Patient 5	Torso phantom	3D printed phantom and thorax holder
Thorax vertical dimension (mm)	193.2 ± 1.4	205.2 ± 1.6	274.6 ± 1.7	248.9 ± 2.4	259.8 ± 1.3	216.5 ± 1.7	200.0 ± 0.5
Thorax horizontal dimension (mm)	321.5 ± 0.8	307.7 ± 3.2	362.7 ± 2.4	365.4 ± 2.8	389.4 ± 1.4	322.2 ± 1.1	300.0 ± 0.4
Right lung vertical dimension (mm)	145.4 ± 2.0	137.5 ± 1.8	196.0 ± 1.7	158.5 ± 3.8	176.7 ± 1.1	155.1 ± 1.4	150.0 ± 0.6
Right lung horizontal dimension (mm)	100.6 ± 0.9	96.0 ± 0.7	103.9 ± 0.8	98.4 ± 1.6	102.7 ± 1.0	104.5 ± 1.0	103.0 ± 0.4
Sex	female	male	male	female	male	–	–
BMI (kg/m^2)	18.5	18.8	23.5	24.2	24.8	–	–
Average mAs	27.5 ± 0.0	29.8 ± 0.7	57.3 ± 2.5	62.5 ± 3.5	66.9 ± 2.2	27.5 ± 0	31.6 ± 0.0
$CTDI_{vol}$ (mGy)	1.9	2.1	4.1	4.4	4.7	1.9	2.2

properties to blood [23]. Materials with appropriate attenuation properties should be combined with the 3D printing technique such as to render the desired anatomical details and resolution in anthropomorphic phantoms.

Another approach to create 3D printed phantoms is to use segmented anatomy parts of interest from patient images as a starting model. This approach is limited by the resolution of the imaging system used and also the acquisition and reconstruction parameters. Thus, this also limits the use of these phantoms to verify the capabilities of the imaging systems. Leng et al developed phantoms based on patient images of the liver and the brain in this way [39]. Hazelaar et al created a thorax phantom containing vessels (> 1 mm diameter) based on patient images, which they 3D printed as different sections that were later put together [40]. The material they used for the vessels (also for the airways and outer lung surface) was nylon, with an average attenuation of –378 HU, which is lower than the values observed in patients. The approach used in our study and in the study by Solomon et al, based on generating a mathematical model for the phantoms (compared to using patient CT images as input), enables to have control over the model or design reference standard without being degraded or limited by blur or resolution of an imaging system [8,9].

One of the aspects that still have to be investigated is the accuracy and reproducibility of the 3D printing process. As far as we know, this issue has not been investigated yet in other publications related to 3D printed phantoms for medical imaging [8,9]. During the printing and curing process some vessels of the phantom might not have been created accurately compared to the model. At the stage where the support material is removed from the model, small vessels could have broken. A recent study, in which an anthropomorphic thorax phantom was created for positional verification purposes in radiotherapy, applied a surface comparison using the STL models of the different sections forming the phantom as a gold standard which was compared to segmented volumes for each section extracted from CT images using commercial software (GOM Inspect metrology software) [40,41]. In our study, simple measurements were taken on one of the bigger vessels in the 3D printed phantom with a Vernier caliper, with an average diameter of (8.51 ± 0.05) mm, which is compatible with the expected value from the design file (8.50 mm). The accuracy and reproducibility of the 3D printing process will be investigated more thoroughly in a future study.

CT standards for image quality, including national and international guidelines and manufacturers specifications, are established based on the analysis of images of uniform phantoms containing patterns to derive image quality metrics such as noise, contrast-to-noise ratio, uniformity, linearity, noise power spectrum (NPS), Modulation Transfer Function (MTF), among others. These metrics characterize fundamental aspects of image quality related to the technical performance of the CT system in quality controls. These technical measurements are well described, well known by the medical physics community, reproducible and widely accepted as a standard. They are useful for constancy test, specifications check and testing that systems perform within acceptable thresholds [42,43]. The geometric phantoms used in combination with these metrics do not reproduce, in general, the patient's anatomy or attenuation and the measured parameters do not relate with the specific clinical tasks performed by the radiologists. Moreover, predicting clinical image quality in patient images, based on the results provided with these methodologies, is not straightforward [6]. The use of anthropomorphic phantoms (based on 3D printing or other techniques) in combination with these widely accepted metrics or newly developed ones, represents a step forward to analyze image quality in conditions closer to the clinical practice with patients. This is especially relevant in CT, due to the non-linear properties of manufacturer dependent iterative reconstruction algorithms, which in some cases rely on patient anatomical models.

3D printing is a low-cost alternative to develop phantoms for image quality assessment in medical applications. For instance, compared to the costs of off-the shelf commercial phantoms (approximately, as the price varies between providers and countries), the 3D printed lung vessel phantom (together with the PMMA thorax shaped holder) costs a few hundred euros. Geometric image quality phantom, such as Catphan cost of the order of ten thousands of euros and anthropomorphic detailed phantoms (like the commercial thorax phantom) of the order of several tens of thousands of euros. It has to be noted that the Kyoto Kagaku torso phantom, for instance, offers detailed organs also for other parts of the body (head, thorax and abdomen) and the Catphan phantom includes several modules to assess different aspects of image quality, whereas the designed 3D printed lung vessel phantom can only be used to assess image quality for thorax protocols so far.

Filippou et al, in a systematic review of papers related to 3D printed phantoms for medical imaging, in particular 50 considered relevant, including phantoms developed for CT, PET, SPECT (combining water tight phantoms with radiotracers), mammography, MRI, US or multimodality [12]. The evaluated parameters to analyze the properties of the phantoms depended on the imaging modality, being the most common Hounsfield units, density, X-ray attenuation and speed of sound. The phantoms design ranges from anthropomorphic phantoms mimicking organs (such as liver or breast) or whole parts of the body (head or torso phantoms, 3D printed phantoms modifying off-the shelf phantoms) or geometric phantoms containing customized object patterns [12]. This research topic is evolving fast and future developments could go in the direction of multimodality image quality phantoms, dynamic phantoms to assess the performance of motion correction software, or using biomaterials based on protein synthesis to analyze physiological processes.

The main use of the 3D printed lung phantom is to assess image quality in CT. In another study published elsewhere by our group, this was accomplished combining CT images of the phantom and the phantom design using an objective image quality metric, the structural similarity index (SSIM) [44]. Images of the phantom were acquired at different dose levels and reconstructed with three reconstruction algorithms [13]. The SSIM values were lower as the dose decreased and also varied between reconstructions. This application has the potential to be used in protocol optimization.

Another purpose of the 3D printed phantom is to be used together with objects as surrogates for lung nodules in combination with a model observer for image quality assessment [45,46]. Model observers are mathematical algorithms that aim at reproducing human performance in simple detection and discrimination tasks and have been successfully applied to detect objects in uniform surroundings [47]. The effect of structural backgrounds (such as the lung vessels and parenchyma) in CT on the performance of such models compared to humans is yet to be investigated [46].

5. Conclusions

A 3D printed lung phantom containing a complex structure of vessels was designed and manufactured to be used in image quality assessment in CT. CT images of the phantom, inside a holder as a surrogate of the thorax were compared to patient images and a commercial torso phantom in terms of vessels distribution and attenuation. The attenuation of the materials used for the vessels and the thorax shaped holder is within the range of the attenuations observed in patients, though future effort will be put into finding new materials to mimic these values more accurately and to simulate the parenchyma. The continual improvement in 3D printing methods and materials' attenuation range makes this technology an alternative to off-the shelf phantoms to create low cost, customized phantoms, that can be tailored to more robust and accurate patients' anatomy or disease staging models. This approach can lead to image quality assessment closer to the clinical image quality scenario considering variations in the patients' anatomy, morphometry and pathology.

Acknowledgements

The 3D printed lung phantom was developed inside the CLUES project (http://www.clues-iq.blogspot.com/p/main-page.html) funded by the Dutch Technology Foundation NWO-TTW (grant number 13592).

References

[1] Tack D, Kalra MK, Genevois PA, editors. Radiation dose from multidetector CT. 2nd ed.Springer-Verlag; 2012.
[2] Radiation Protection n°180. Medical radiation exposure of the European population. Luxembourg: Publications Office of the European Union; 2015. doi: 10.2833/708119.
[3] Kanal KM, Butler PF, Sengupta D, Bhargavan-Chatfield M, Coombs LP, Morin RLUS. Diagnostic Reference Levels and achievable doses for 10 adult CT examinations. Radiology 2017;284(1):120–33.
[4] Beister M, Kolditz D, Kalender WA. Iterative reconstruction methods in X-ray CT. Phys Med 2012;28:94–108.
[5] Geyer LL, Schoeph UJ, Meinei FG, Nance JW, Bastarrika G, Leipsic JA. State of the art: Iterative CT reconstruction techniques. Radiology 2015;276(2):339–57.
[6] Verdun FR, Racine D, Ott JG, Tapiovaara MJ, Toroi P, Bochud FO, et al. Image quality in CT: from physical measurements to model observers. Phys Med 2015;31(8):823–43.
[7] Xie George Xu, Eckerman Keith F, editors. Handbook of anatomical models for radiation dosimetry. Boca Raton, FL: ECR Press, Taylor & Francis; 2010.
[8] Solomon J, Bochud F, Samei E. Design of anthropomorphic textured phantoms for CT performance evaluation. Proc SPIE Medical Imaging 2014;9033:90331U.
[9] Solomon J, Samei E. Quantum noise properties of CT images with anatomical textured backgrounds across reconstruction algorithms: FBP and SAFIRE. Med Phys 2014;41:091908.
[10] Solomon J, Ba A, Bochud F, Samei E. Comparison of low-contrast detectability between two CT algorithms using voxel-basd 3D printed textured phantoms. Med Phys 2016;43(12):6497–506.
[11] Gear JI, Cummings C, Craing AJ, Divoli A, Long CDC, Tapner M, et al. Abdo_Man: a 3D-printed anthropomorphic phantom for validating quantitative SIRT. EJNMMI Phys 2016:3–17.
[12] Filippou V, Tsoumpas C. Recent advances on the development of phantoms using 3D printing for imaging with CT, MRI, PET, SPECT and ultrasound. Med Phys 2018;45(9):e740–59.
[13] Joemai RMS, Geleijns J. Assessment of structural similarity in CT using filtered backprojection and iterative reconstruction: a phantom study with 3D printed lung vessels. Br J Radiol 2017;90:20160519.
[14] Weibel ER, Gomez DM. Architecture of the human lung. Use of quantitative methods establishes fundamental relations between size and number of lung structures. Science 1962;137(3530):577–85.
[15] Weibel ER. What makes a good lung? Swiss Med Wkl 2009;139(27–28):375–86.
[16] 3D slicer software https://www.slicer.org/.
[17] Meshlab software http://meshlab.sourceforge.net/.
[18] Freecad software https://www.freecadweb.org/.
[19] CT Torso Phantom CTU-41 Kyoto Kagaku https://www.kyotokagaku.com/products/detail03/pdf/ph-4_manual.pdf.
[20] Vardhanabhuti V, Olubaniyi B, Loader R, Riordan RD, Williams MP, Roobottom CA. Image quality assessment in torso phantom comparing effects of varying automatic current modulation with filtered back projection, adaptive statistical, and model-based iterative reconstruction techniques in CT. J Med Imag Radiat Sci 2012;43(4):228–38.
[21] ImageJ software https://imagej.nih.gov/ij/.
[22] Adaptive active contours (snakes) for the segmentation of complex structures in biological images. Philippe Andreya and Thomas Boudierb ImageJ conference 2006. Available at: http://imagejdocu.tudor.lu/doku.php?id=plugin:segmentation:active_contour:start.
[23] International Commission on Radiation Units and Measurements. Report 44 of the International Commission on Radiation Units and Measurements (Bethesda, MD); 1989.
[24] Huang W, Yen RT, McLaurine M, Bledsoe G. Morphometry of the human pulmonary vasculature. J Appl Physiol 1996;81(5):2123–33.
[25] Madamesilla J, McGeachy P, Villareal Barajas E, Khan R. Phys Med 2016;32:242–7.
[26] Dancewicz OL, Sylvander SR, Markwell TS, Crowe SB, Trapp JV. Radiological properties of 3D printed materials in kilovoltage and megavoltage photom beams. Phys Med 2017;38:111–8.
[27] AAPM Special Interest Group in 3D printing (https://www.rsna.org/3D-Printing-SIG/).
[28] Kairn T, Crowe SB, Markwell T. Use of 3D printed materials as tissue-equivalent phantoms. In World Congress on Medical Physics and Biomedical Engineering 2015, Toronto, Canada: IFMBE Proceedings 51.
[29] Kapetanakis I, Fountos G, Michail C, Valais I, Nalyvas N. 3D printing X-ray quality control phantoms. A low contrast paradigm. IOP Conf Series: J Phys: Conf 2017:931. 012026.
[30] Multipurpose Chest Phantom N1 “LUNGMAN” https://www.kyotokagaku.com/products/detail03/ph-1.html.
[31] Stoel BC, Stolk J. Optimization and standardization of lung densitometry in the assessment of pulmonary emphysema. Invest Radiol 2004;39(11):681–8.
[32] Solomon JB, Samei E. Are uniform phantoms sufficient to characterize the performance of iterative reconstruction in CT? Proc. Of SPIE Vol. 8668 86684M-1-6 Medical Imaging 2013 (Physics of Medical Imaging).
[33] Antrhopomorphic thorax phantom QRM http://www.qrm.de/content/products/anthropomorphic/thorax_phantom.htm.
[34] Kitaoka H. Computational morphology of the lung and its virtual imaging. Eur J Radiol 2002;44:164–71.
[35] Burrowes KS, Hunter PJ, Tawhai MH. Anatomically based finite element models of the human pulmonary arterial and venous trees including supernumerary vessels. J Appl Physiol 2005;99:731–8.
[36] Abadi E, Segars WP, Sturgeon GM, Roos JE, Ravin CE, Samei E. Modeling lung architechture in the XCAT series of phantoms: physiologically based airways, arteries and veins. IEEE TMI 2018;37(3):693–702.
[37] Ivanov D, Bliznakova K, Buliev I, Popov P, Mettivier G, Russo P. Suitability of low density materials for 3D printing of physical breast phantoms. Phys Med Biol 2018;63:175020.
[38] Alssabbagh M, Aziz Tajuddin A, Manap MBA, Zainon R. Evaluation of nine 3D printing materials as tissue equivalent materials in terms of mass attenuation coefficient and mass density. IJAAS 2017;4(9):168–73.
[39] Leng S, McGee K, Morris J, Alexander A, Kuhlmann J, Vrieze T, et al. Anatomic modeling using 3D printing: quality assurance and optimization. 3D Print Med 2017;3:6.
[40] Hazelaar C, van Eijnatten M, Dahele M, Wolff J, Forouzanfar T, Slotman B, et al. Using 3D printing techniques to create an anthropomorphic thorax phantom for medical imaging purposes. Med Phys 2018;45(1):92–100.
[41] GOM software http://www.gom.com/3d-software/gom-inspect.html.
[42] International standard: IEC 61223-3-5. Evaluation and routine testing in medical imaging departments – part 3–5: acceptance tests – imaging performance of computed tomography X-ray equipment; 2004.
[43] Gilliksrud K, Stokke C, Martinsen ACT. How to measure CT image quality: Variations in CT-numbers, uniformity and low contrast resolution for a CT quality assurance phantom. Phys Med 2014;30(4):521–6.
[44] Wang Z, Bovik AC, Sheikh HR, Simoncelli EP. Image quality assessment: from error visibility to structural similarity. IEEE Trans Image Process. 2004;13(4):600–12.
[45] Hernandez-Giron I, Geleijns J, Calzado A, Veldkamp WJH. Automated assessment of low contrast sensitivity for CT systems using a model observer. Med Phys 2011;38(S1):S25–35.
[46] Hernandez-Giron I, Veldkamp WJH, Streekstra GJ. Towards automated clinical image quality assessment in CT: 3D model observer applied to simulated images of a virtual lung phantom. Abstract presented at the European Conference of Radiology (ECR), Vienna 2017 (B-0653). Book of abstracts. Insights Imaging 2017;8(Suppl 1). https://doi.org/10.1007/s13244-017-0546-5.
[47] Hernandez-Giron I, Geleijns J, Streekstra GJ, Veldkamp WJH. Framework for objective clinical image quality assessment in thorax CT: A 3D model observer in combination with a 3D printed lung phantom containing nodules. Presented at: Radiological Society of North America (RSNA) 2017 Scientific Assembly and Annual Meeting, November 27-December 2, 2017, Chicago, IL. (SSG15-06).